

Article

Increasing the Resolution and Spectral Range of Measured Direct Irradiance Spectra for PV Applications

Gabriel López ^{1,*}, Christian A. Gueymard ², Jesús Polo ³, Joaquín Alonso-Montesinos ^{4,5}, Aitor Marzo ⁶, Nuria Martín-Chivelet ³, Pablo Ferrada ⁷, Martha Isabel Escalona-Llaguno ⁸ and Francisco Javier Batllés ^{4,†}

¹ Departamento Ingeniería Eléctrica y Térmica, de Diseño y Proyectos, Escuela Técnica Superior de Ingeniería, Universidad de Huelva, 21007 Huelva, Spain

² Solar Consulting Services, Colebrook, NH 03576, USA

³ Photovoltaic Solar Energy Unit (CIEMAT), 28040 Madrid, Spain

⁴ Departamento Química y Física, Universidad de Almería, 04120 Almería, Spain

⁵ CIESOL, Joint Centre of the University of Almería-CIEMAT, 04120 Almería, Spain

⁶ Departamento Óptica, Universidad de Granada, 18071 Granada, Spain

⁷ Centro de Desarrollo Energético Antofagasta (CDEA), Universidad de Antofagasta, Antofagasta 1240000, Chile

⁸ Universidad Autónoma de Zacatecas, Zacatecas 98000, Mexico

* Correspondence: gabriel.lopez@die.uhu.es

† Deceased.

Abstract: The spectral distribution of the solar irradiance incident on photovoltaic (PV) modules is a key variable controlling their power production. It is required to properly simulate the production and performance of PV plants based on technologies with different spectral characteristics. Spectroradiometers can only sense the solar spectrum within a wavelength range that is usually too short compared to the actual spectral response of some PV technologies. In this work, a new methodology based on the Simple Model of the Atmospheric Radiative Transfer of Sunshine (SMARTS) spectral code is proposed to extend the spectral range of measured direct irradiance spectra and to increase the spectral resolution of such experimental measurements. Satisfactory results were obtained for both clear and hazy sky conditions at a radiometric station in southern Spain. This approach constitutes the starting point of a general methodology to obtain the instantaneous spectral irradiance incident on the plane of array of PV modules and its temporal variations, while evaluating the magnitude and variability of the abundance of atmospheric constituents with the most impact on surface irradiance, most particularly aerosols and water vapor.

Keywords: solar spectral irradiance; SMARTS; PV; atmospheric constituents; soiling



Citation: López, G.; Gueymard, C.A.; Polo, J.; Alonso-Montesinos, J.; Marzo, A.; Martín-Chivelet, N.; Ferrada, P.; Escalona-Llaguno, M.I.; Batllés, F.J. Increasing the Resolution and Spectral Range of Measured Direct Irradiance Spectra for PV Applications. *Remote Sens.* **2023**, *15*, 1675. <https://doi.org/10.3390/rs15061675>

Academic Editor: Filomena Romano

Received: 10 February 2023

Revised: 13 March 2023

Accepted: 17 March 2023

Published: 20 March 2023



Copyright: © 2023 by the authors. Licensee MDPI, Basel, Switzerland. This article is an open access article distributed under the terms and conditions of the Creative Commons Attribution (CC BY) license (<https://creativecommons.org/licenses/by/4.0/>).

1. Introduction

The efficiency and power production of photovoltaic (PV) modules depends on the spectral distribution of the incoming solar irradiance. This dependence is not the same for each of the different technologies used in existing PV cells because of their differing relative spectral response (SR). Because of this technology-specific spectral response, a PV module's efficiency according to the manufacturer under ideal Standard Test Conditions (STCs) can be far from the real response of the module when operating under real weather conditions. Accordingly, several authors [1–4] found that the solar spectral distribution is a key parameter driving the outdoor performance of several types of PV cells. Theoretical studies have also been undertaken to analyse the impact of the incoming solar spectral distribution on the energy yield delivered by different PV technologies. Results show remarkable differences in the PV power generated, mainly when the energy production is evaluated at time scales shorter than a month [5].

In addition to the atmospheric constituents that determine the magnitude and distribution of the solar spectrum, such as aerosols or water vapor, it is now known that the

amount of soiling on the PV modules can also be a factor affecting the spectral irradiance transmitted through their cover [6]. Experiments have been conducted during the last few years to analyse the impact of dust and soiling on the transmission of the incident solar radiation, both at the spectral level and over the entire waveband to which the PV cell responds. It has been found that the transmittance of soiling accumulated on PV modules shows spectral dependence, mostly affecting the shorter wavelengths (ultraviolet and visible) [7–9] and having a significant impact overall. For instance, large broadband transmittance reductions (up to 50%) have been reported in the literature for the soiled cover of both PV panels and flat-plate thermal collectors [10,11].

To account for the effects of the difference between the actual instantaneous incident spectrum and the ideal reference spectrum used for PV ratings at STCs, a spectral mismatch correction factor (or, for short, spectral factor, SF) needs to be determined when simulating the modules' performance under actual conditions. Hence, SF constitutes an important variable to consider for yield analyses of any PV power plant [12,13]. From a modelling standpoint, the use of sunphotometer data, satellite retrievals of atmospheric data, and an appropriate spectral radiation model makes determination possible, albeit usually under clear-sky conditions only. Polo et al. [14] have recently generalized this approach by generating a typical meteorological year of spectral global tilted irradiance, hence creating the means to analyse the effects of spectral irradiance variations on PV performance under all sky conditions. Another possible avenue is to use gridded databases of satellite-derived spectral irradiance estimates. The results of a recent study [15] show that this approach is promising but still has significant uncertainties and is currently not applicable worldwide.

In parallel, experimental determinations of SF are difficult in practice because the wavelength range (e.g., 350 nm to 1050 nm, or at best 300 nm to 1100 nm) of the most common spectroradiometers in current use is shorter than the spectral response of some PV technologies (such as polycrystalline silicon, copper indium diselenide, lattice-matched germanium-based, or multijunction cells used in concentrating PV applications), which can be sensitive up to $\approx 2 \mu\text{m}$ [16,17]. Figure 1 shows the relative spectral response of seven PV technologies (as described in [5]) with wavelengths ranging from 300 nm to 1350 nm along with a common solar direct irradiance spectrum ($G_{b\lambda}$) measured in this work with a commercial spectroradiometer. The latter's wavelength range is limited to 350–1050 nm and is thus not appropriate to evaluate the precise SF of most PV cells. Hence, the effect of the solar spectral distribution on the PV energy production cannot be accurately analysed with this typical instrumentation. The commercial combinations of two or more spectroradiometers do exist to achieve a much larger spectral range, as used at a small number of laboratories (see, e.g., [15]); however, the additional instrumentation is very costly, which makes it unavailable for most institutions.

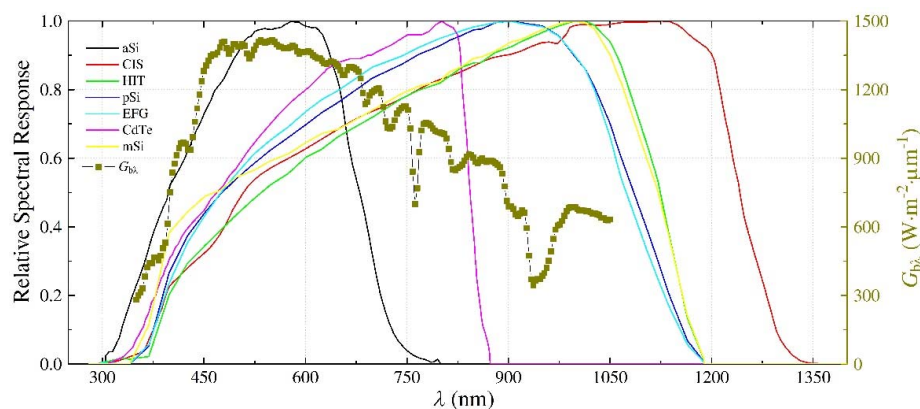


Figure 1. Relative spectral responses of seven PV technologies (left y-axis) over the 300–1350 nm waveband. The direct solar spectral irradiance $G_{b\lambda}$ measured at Huelva (Spain) with a tracking spectroradiometer at 1200 UT on 2021-03-24 is shown for reference (right y-axis).

Based on the above considerations, it appears that the ideal experimental avenue would require either spectroradiometers covering a wider spectral range (with the inconvenience of increasing costs) or the development of algorithms that would expand the limited spectrum sensed by usual spectroradiometers and provide a reasonable irradiance estimate over the entire shortwave spectrum. Here, the latter hybrid (measurement + model) approach is explored, using a new methodology based on the Simple Model of the Atmospheric Radiative Transfer of Sunshine (SMARTS) spectral code (version 2.9.8) [18] to achieve four complementary goals: (i) extend the wavelength range of measured direct irradiance spectra from ≈ 1050 nm up to 4000 nm; (ii) substantially improve the spectral resolution of the spectroradiometers (typically 7–10 nm) to 1 nm for the end product; (iii) provide accurate estimates of the clear-sky broadband irradiances incident on horizontal or tilted planes; (iv) evaluate the magnitude and variability of the abundance of various atmospheric constituents. The latter goal would normally require local (and expensive) remote-sensing instrumentation, which is rarely available at solar laboratories. Since the abundance of key atmospheric constituents, such as aerosols, water vapor, or ozone, must first be retrieved satisfactorily, this constitutes an interesting by-product in itself. In a second step, the expanded spectrum is calculated with SMARTS, using those retrievals.

The SMARTS model's conceptual idea is to offer fast and accurate predictions of spectral irradiance on any tilted surface without the difficulties and limitations associated with the atmospheric models such as MODTRAN [19] or libRadtran [20], which require a large amount of atmospheric information that is often unavailable at the site of interest. The SMARTS model is now widely used worldwide in a large variety of applications. This is made possible by the model's versatility and accuracy, which has been abundantly validated [21–23]. The model currently accommodates the case of cloudless skies only, for which it evaluates the clear-sky spectral irradiances (direct beam, circumsolar diffuse, hemispherical diffuse, and total on a prescribed receiver plane—tilted or horizontal) for specific atmospheric conditions (user specified or selected from 10 standard atmospheres), and for one-to-many points in time or solar geometries. The algorithms were developed to match the output from the sophisticated MODTRAN band models within $\approx 2\%$. The algorithms are implemented in compiled FORTRAN code for various platforms and are used in conjunction with data files describing the spectral variation of surface albedo and of the absorption of atmospheric components. The spectral resolution is 0.5 nm from 280 nm to 400 nm, 1 nm from 400 nm to 1750 nm, and 10 nm from 1750 nm to 4000 nm. The version 2.9.8 used here is intended for education and research and is free for use for these intended applications.

2. Experimental Setup

The experimental setup is located on a flat building roof of the High Technical School of Engineering on the Campus of La Rábida of the Universidad de Huelva (UHU), near Huelva (southwestern Spain), a seashore site within 5 km of the Atlantic Ocean (Figure 2). The aerosol species that are most frequent over the station region are coastal maritime, rural/continental, pollen, and desert dust [24].

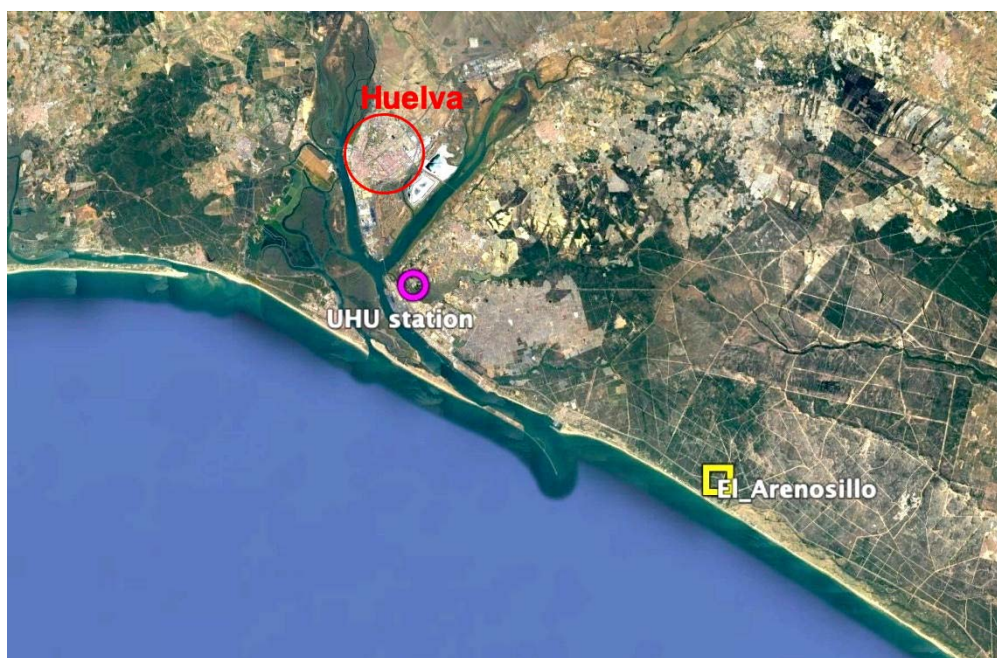


Figure 2. Location of the radiometric and meteorological station of the Universidad de Huelva, Spain (UHU facilities). The city of Huelva and the AERONET station of “El Arenosillo” are also indicated.

The experimental dataset consists of values of spectral beam normal irradiance ($G_{b\lambda}$), broadband global horizontal (G), broadband diffuse horizontal (G_d), and broadband direct normal (G_b) irradiances, as well as all-sky images and meteorological data (temperature, relative humidity, pressure, and wind speed), all of which have been collected since December 2020. $G_{b\lambda}$ is measured at 5-min resolution using an MS-700N (EKO Instruments Co. Ltd., Tokyo, Japan) spectroradiometer equipped with a collimation tube. The instrument’s detector is a CCD array that covers the spectral range from 350 nm to 1050 nm with a wavelength interval of ≈ 3.3 nm, a spectral resolution of 10 nm, and a wavelength accuracy better than 0.3 nm. An EKO MS-56 pyrheliometer and two EKO MS-802 pyranometers (one of them blocking the sun by means of a shadow ball), separately sense the three essential components of solar radiation (G_b , G , and G_d , respectively). The spectral ranges that are sensed by the pyrheliometer and the pyranometers are (200–4000 nm) and (285–3000 nm, before absolute calibration), respectively. All these radiometers are mounted on an EKO STR-22G sun tracker.

The meteorological variables are measured with a WD-500 sensor manufactured by Lufft GmbH (Fellbach, Germany), and the sky images are taken using an EKO CMS ASI-16 All-Sky Imager. The latter is an automatic all-weather camera system with 180° field of view, using a 5-MP camera and a fish-eye lens with an anti-reflective, airflow protected, quartz dome. It delivers high-resolution images of the sky and clouds with a resolution of 1920 \times 1920 pixels and 8-bit resolution per pixel. The horizon as seen by the ASI-16 is completely unshaded because the surroundings are at lower elevation.

Figure 3 shows the experimental setup, as installed on the flat roof of the building. The radiometric variables are sampled each second and are reported as 1-min averages. In parallel, the all-sky images and meteorological parameters are sampled every minute. All sensors are cleaned three days a week in the morning. Intercomparisons with unused radiometric sensors and several tests are carried out to guarantee the continuous quality of the broadband solar radiation measurements. The spectroradiometer is assumed to keep the original uncertainty provided by the manufacturer ($<\pm 18\%$ for short wavelengths, improving to $<\pm 5\%$ over the central part of the spectral range), or at least with an insignificant degradation of calibration, because the experimental period is short (less than two years, which is the calibration interval recommended by EKO).



Figure 3. Radiometric and meteorological station of the Universidad de Huelva at the La Rábida Campus. The spectroradiometer and the pyrheliometer (at the left) and the all-sky imager (at the right) are marked with red rectangles.

Since one of the intermediate results derived from this work is the determination of some key aerosol optical properties (i.e., the aerosol optical depth at 500 nm, AOD_{500} , and the Ångström exponent, α) as well as the amount of water vapor (expressed as precipitable water, PW), the reference determinations of these variables were also obtained from a CE318 sunphotometer from Cimel (Paris, France), belonging to the AERONET network [25]. This instrument is located at the El Arenosillo Atmospheric Sounding Station (Instituto de Técnica Aeroespacial, INTA) in Mazagón (Huelva), another seashore site only ≈ 20 km away from the Campus of La Rábida. Figure 2 shows the location of the two stations.

Although many days of valid data are available, the present study focuses on only two cloudless days with very contrasting turbidity situations: one with a very clear sky (2021-03-24), characterized by minor aerosol load and low aerosol optical depth (AOD), and the other corresponding to hazy (highly turbid) conditions (2021-04-04). These sky conditions were selected manually by means of visual inspection of the daily evolution of solar radiation components and sky images (Figures 8 and 9). This process is time-consuming, which is why a long period of time (i.e., several months) is not included here. Nevertheless, an automatic procedure to discriminate between haze and cloudiness is currently being developed using the all-sky camera images [26]. This procedure is intended to become a reference for the selection of true cloudless sky conditions, in comparison with purely radiometric methods, which typically introduce some uncertainty [27]. In any case, a total of 20 spectra is used in this work to exemplify the procedure. Each experimental spectrum is sensed at 212 wavelengths, resulting in a total of 4240 spectral points. Nearly all of them are actively used in the retrieval procedure to extract the atmospheric properties of the moment. Hence, this amount is considered enough to ensure the reliability of the proposed methodology.

Remarkably, the atmospheric conditions that existed during the experiments at the UHU station also prevailed over the whole area of interest, including where the INTA-AERONET sunphotometer is located, as confirmed by the inspection of spaceborne imagery (such as those obtained using the EUMETSAT platform [28]) and aerosol data from MODIS. In this respect, Figure 4 (top) shows the area of interest (delimited by a red rectangle) as viewed by the Meteosat SEVIRI radiometer using an RGB natural-colour-enhanced product for one of the days selected in this work (2021-03-24) at 0915 UT. The presence of clouds is noted inside the red rectangle. The ASI-16 All-Sky Imager is also able to sense the sky over the El Arenosillo station. Figure 4 (bottom) shows a sky image corresponding to the same day and instant. Three circles are added, denoting three heights above ground (1.5 km,

5 km, and 7 km) and at a horizontal distance of 20 km from the imager. A green line marks the view direction to the El Arenosillo station. Low-level clouds over El Arenosillo would stand on the red circle at a mean height of \approx 1.5 km above ground; mid-level clouds located at a mean height of \approx 5 km would be seen on the yellow circle, and high-level clouds at \approx 7 km would appear on the black circle. Nevertheless, the distance of clouds cannot be precisely determined from such sky images, since clouds at different horizontal distances from the All-Sky Imager with the same elevation angles are projected into the same pixel. However, if no clouds are present in the sky image, the same cloudless conditions would exist at both locations.

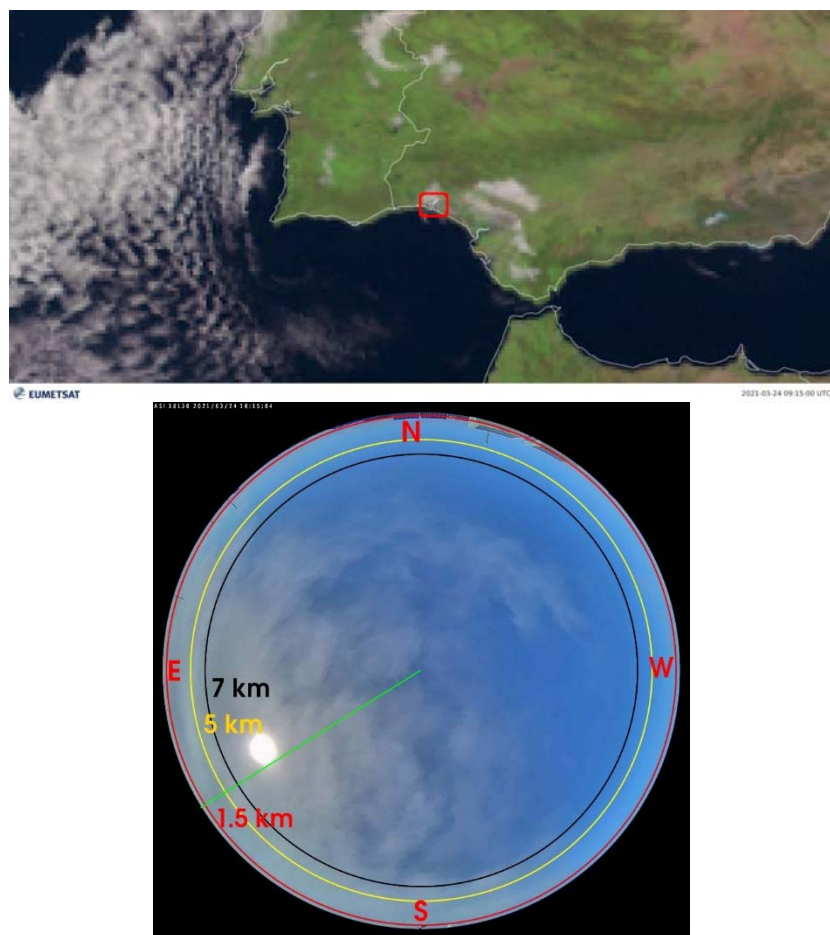


Figure 4. TOP: Satellite image showing most of southwestern Spain for 2021-03-24 at 0915 UT. The Universidad de Huelva (UHU) and El Arenosillo stations are inside the red rectangle. Some clouds are detected over both sites. BOTTOM: Sky image from the All-Sky Imager instrument located at the UHU radiometric station for the same day and instant as the satellite image above. Three circles denote three possible cloud layers (low-, medium-, and high-level clouds) at a horizontal distance of 20 km from the camera. A green line is added to mark the view direction to the El Arenosillo station.

3. Methodology

The novel methodology proposed here attempts to obtain the specific values of the inputs to SMARTS that can, in turn, generate the modelled direct spectra that best fit their experimental counterpart. To this end, the variables to be estimated are either determined analytically or through a multistep iterative process, where they are varied incrementally between specific minimum and maximum limits until an optimum combination is found. Ultimately, for each instant when a measured spectrum is available, the modelled spectrum that is eventually selected is the one that results in the lowest root-mean-square error in comparison with its measured counterpart.

Each experimental direct spectrum is analysed to provide information about the atmospheric constituents in a way that is similar to what retrieval algorithms do for sun-photometric observations at, e.g., AERONET stations. In comparison, however, common CCD-array spectroradiometers, as with the one used here, normally have a coarser resolution (with irradiance at nearby wavelengths affecting each other) and are not calibrated against the sun; thus, they have a larger absolute uncertainty. These adverse conditions are compensated for here by using the guidance of a radiative transfer model and developing an appropriate iterative method. To be valid, the experimental spectra must be obtained under sky conditions characterized by a *clear line of sight* to the sun. This specific situation is comparable to what is obtained in similar remote-sensing (AERONET) retrievals after cloud screening, i.e., at level 1.5. This sky condition is much less stringent than a fully *cloudless* sky. Nevertheless, the latter prerequisite is actually implemented in this work for validation purposes because one way of verifying the method (see Section 4) consists of comparing the calculated and measured broadband diffuse and global irradiances, which are both very sensitive to cloudiness anywhere in the sky. For that specific purpose, the clear-sky condition is verified by visual inspection of the temporal variation of each broadband solar radiation component as well as by all-sky images. In the absence of an all-sky imager, both the cloudless and clear line-of-sight conditions can be identified a posteriori from broadband irradiance records using an advanced clear-sky detection algorithm [27].

The key inputs being incrementally varied in SMARTS, as well as their current acceptable limits, are given in Table 1. Gueymard's synthetic extraterrestrial spectrum ($G_{0\lambda}$) [29] is selected, corresponding to a solar constant of 1361.1 W/m^2 . Default values are used for those inputs that do not affect the shortwave direct irradiance: CO_2 abundance (set here to 400 ppmv), aerosol's single scattering albedo and asymmetry parameter (set to 0.9 and 0.7, respectively), and surface albedo (set to Light Soil). The pressure, temperature, and relative humidity inputs are normally measured; however, any missing value is estimated from the latitude and elevation of the site (37.20°N and 20 m a.m.s.l., respectively), along with the reference atmosphere, selected to be Mid-Latitude Summer (MLS) in the present case. The main radiatively active atmospheric quantities (AOD, α , PW, ozone, and air quality) are then derived iteratively to eventually determine the best combination of inputs, as described below.

Table 1. Input values being varied in SMARTS and their range of tolerance for the fitting process.

Precipitable Water Content, PW (cm)	Ozone Content, u_o (cm)	Air Quality (Trace Gases)	Ångström Exponent (α_1, α_2)	Turbidity (AOD ₅₀₀)
0.5–6.0	0.300–0.360	Pristine to Severe pollution	0.1–3.0	0.04–0.40

Figure 5 shows the transmittances corresponding to the atmospheric extinction processes used in SMARTS on 2021-04-04 at 0700 UTC. That specific low-sun moment (soon after sunrise) is characterized by an air mass (AM) higher than 5. This critical situation is intentionally selected here to observe the atmospheric effects on solar radiation when all extinction processes are enhanced by the longer atmospheric path. The transmittances provided by SMARTS are separately calculated for molecular (Rayleigh) scattering, T_r , ozone absorption, T_o , trace gases absorption, T_{tg} , mixed-gas absorption, T_{mg} , water vapor absorption, T_w , and aerosol scattering, T_a . The SMARTS spectral grid (2002 wavelengths between 280 nm and 4000 nm) has much finer intervals than the MS-700N grid (212 wavelengths between 350 nm and 1050 nm); moreover, the latter's spectral resolution ($\approx 10 \text{ nm full width at half maximum, FWHM}$) is much coarser than that of SMARTS. Hence, the smoothing of all SMARTS spectral outputs (through the application of an appropriate gaussian filter) is always necessary when any comparison with an experimental spectrum is made. Following this procedure, the SMARTS transmittances and spectra are progressively modified to closely match the experimental spectra provided by the spectroradiometer. A

total of 212 observed spectral data points per spectrum is finally obtained between 350 nm and 1050 nm.

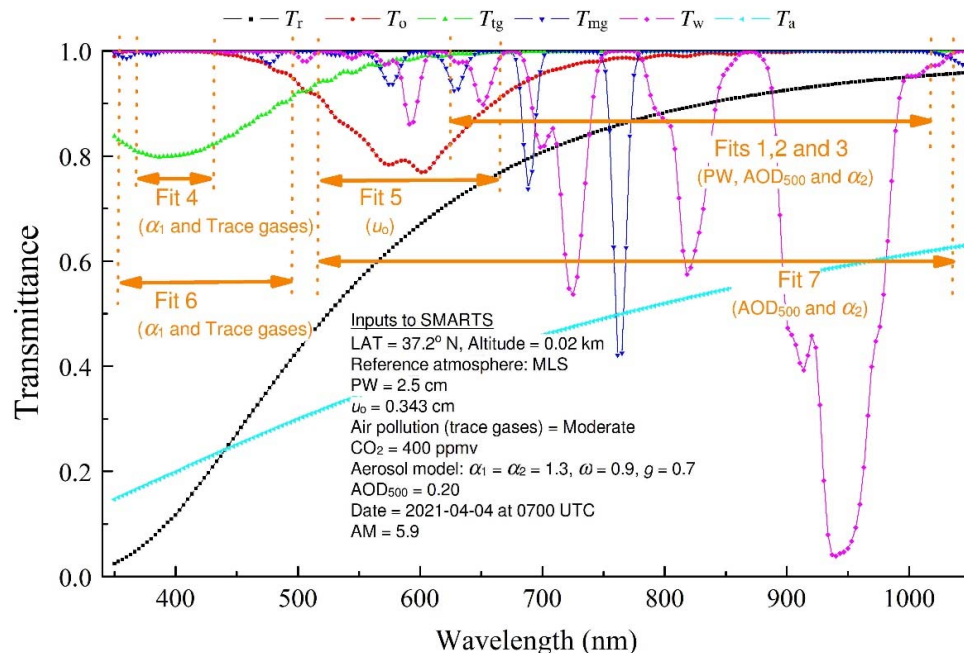


Figure 5. Atmospheric transmittances obtained using SMARTS for molecular scattering (Rayleigh scattering) T_r , ozone absorption T_o , trace gases absorption T_{tg} , mixed gases absorption T_{mg} , water vapor absorption T_w , and aerosol extinction T_a , per the colour code. The specific inputs are given explicitly. The orange arrows indicate the spectral bands selected for the determination of the atmospheric variables along with the order number of each fitting process involved.

Figure 5 also shows several spectral bands (denoted by orange arrows) that are used as windows to calculate the best estimates for the SMARTS inputs, using an iterative fitting process consisting of 6 steps and 7 iterations, as detailed in the following subsections.

3.1. Step 1

The first step is conducted before the iterative fitting process and is intended to provide an initial and approximate value for both AOD_{500} and the specific Ångström's exponent for $\lambda > 500$ nm: α_2 . The main reason for this preliminary analytic calculation is to save computer time, since an alternate iterative procedure could be excessively long (i.e., more than 10 min per spectrum) because convergence can be slow in that part of the spectrum.

Based on the data used in Figure 5, Figure 6 shows the total absorption transmittance obtained by removing the molecular and aerosol scattering, i.e., $T_{abs} = T_{Total}/T_r \cdot T_a = T_o \cdot T_{tg} \cdot T_{mg} \cdot T_w$. This is calculated over a very short spectral range (864.5–874.4 nm), which actually consists of only four wavelengths in the case of the MS-700N instrument: $\lambda_1 = 864.5$ nm, $\lambda_2 = 867.8$ nm, $\lambda_3 = 871.1$ nm, and $\lambda_4 = 874.4$ nm. Over that waveband (marked with a red rectangle in Figure 6), the total absorption transmittance is remarkably larger than 0.992 because the atmospheric attenuation of direct irradiance is mainly caused by molecular and aerosol scattering. Hence, for those wavelengths:

$$G_{b\lambda} \approx G_{0\lambda} \cdot T_r \cdot T_a = G_{0\lambda} \cdot T_r \cdot \exp(-m_a \cdot AOD_\lambda), \quad (1)$$

where $G_{0\lambda}$ is the extraterrestrial irradiance corrected for the actual sun–earth distance, m_a is the aerosol optical mass, and AOD_λ is the aerosol optical depth at wavelength λ . If measured values of $G_{b\lambda}$ are used, all terms in the above equation are known, except for AOD_λ , since both T_r and m_a are only functions of solar position and pressure. Hence, AOD_λ

can be calculated by solving Equation (1). Furthermore, based on Ångström's equation, AOD_{500} and α_2 can be evaluated if AOD_λ is known at any two wavelengths λ_a and λ_b :

$$\alpha_2 = \frac{\lambda_a}{\lambda_b} \ln \left(\frac{\text{AOD}_{\lambda_a}}{\text{AOD}_{\lambda_b}} \right) \quad (2)$$

$$\text{AOD}_{500} = \text{AOD}_\lambda \left(\frac{\lambda}{500} \right)^{\alpha_2} \quad (3)$$

where wavelengths are expressed in nm. In Equation (2), better accuracy is obtained when λ_a and λ_b are spread as far as possible; hence, $\lambda_a = 864.5$ nm and $\lambda_b = 874.4$ nm. The near-centre wavelength of 867.8 nm is selected for λ . In what follows, these initial values are referred to as $\text{AOD}_{500}(0)$ and $\alpha_2(0)$, respectively. They are ultimately refined at Step 6.

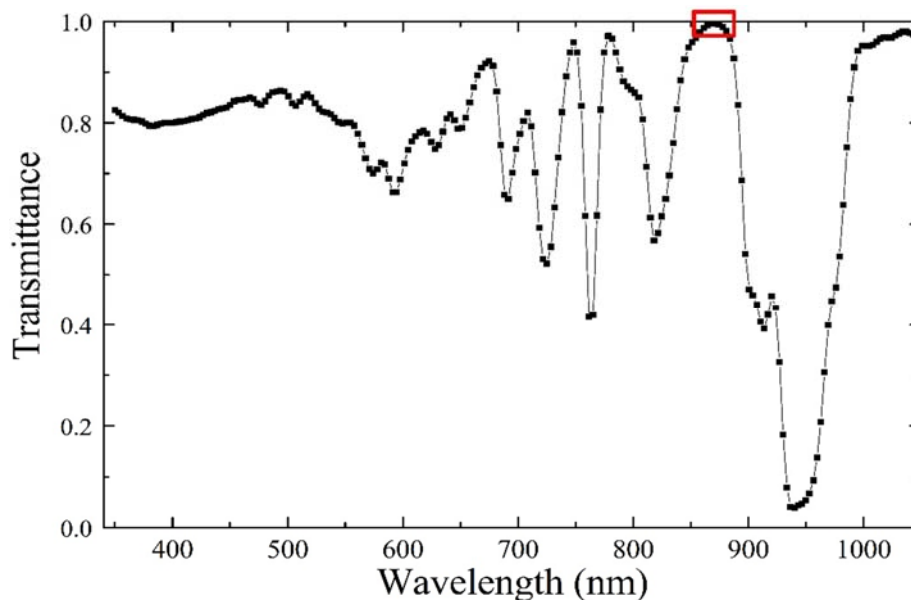


Figure 6. Atmospheric gaseous transmittance, $T_g = T_o \cdot T_{tg} \cdot T_{mg} \cdot T_w$, simulated by SMARTS using the inputs given in Figure 5 for 2021-04-04. A red rectangle is added to highlight a particular spectral band (864.5–874.4 nm) where the atmosphere is almost transparent to solar radiation except for the attenuation processes caused by molecular and aerosol scattering.

3.2. Step 2

The next step is to obtain a preliminary value for PW, and another set of estimates for AOD_{500} and α_2 . The spectral band selected here is 631.4–1011.6 nm, which contains 115 wavelengths in the case of the MS-700N instrument. In that range, the effect of trace gases is negligible (Figure 5). In addition, the ozone transmittance is not sensitive to small variations in total-column ozone abundance, u_o , which is initially set to the value of 0.34 cm that is used to define the reference AM1.5 spectra of STC [30]. Furthermore, the mixed-gas transmittance is well approximated with the selected reference atmosphere of Mid-Latitude Summer (MLS), along with the related inputs of latitude, elevation, date, and time. Two other SMARTS inputs, namely the Ångström exponent α_1 (defined for $\lambda < 500$ nm) and the abundance of trace gases, do not affect the current calculations and are thus defaulted to 1.3 and “light pollution”, respectively. To save computer time, the evaluation of PW, AOD_{500} , and α_2 is carried out by means of three consecutive fits (Fits #1, #2 and #3, as described in Table 2 and shown in Figure 5), where the corresponding intervals and maximum limits of the variables are progressively decreased. These estimates are labelled PW(#3), $\text{AOD}_{500}(\#3)$, and $\alpha_2(\#3)$.

Table 2. Initial values, maximum values, and increments for the estimation of three key SMARTS inputs when using iterative fits. The three consecutive fits are denoted as #1, #2, and #3.

Fit	PW (cm)			AOD ₅₀₀			α_2		
	Initial Value	Max.	Increment	Initial Value	Max.	Increment	Initial Value	Max.	Increment
#1	PW(0) = 0.5	6.0	0.5	AOD ₅₀₀ (0)	—	—	$\alpha_2(0) - 0.5$	$\alpha_2(0) + 0.5$	0.1
#2	PW(#1) − 0.25	PW(#1) + 0.25	0.05	AOD ₅₀₀ (0) − 0.06	AOD ₅₀₀ (0) + 0.06	0.030	$\alpha_2(#1) - 0.25$	$\alpha_2(0) + 0.25$	0.02
#3	PW(#2) − 0.05	PW(#2) + 0.25	0.01	AOD ₅₀₀ (0) − 0.015	AOD ₅₀₀ (0) + 0.015	0.005	$\alpha_2(#2) - 0.05$	$\alpha_2(0) + 0.05$	0.015

3.3. Step 3

The next unknowns to be estimated are α_1 and the trace-gases abundance. Figure 5 shows that there is a specific spectral band below 500 nm (namely, 369.9–426.8 nm), where the only attenuation is caused by aerosols and trace gases, because that of water vapor, ozone, and mixed gases is negligible. In this case, the fourth iterative fit (Fit #4 in Figure 5) is performed by varying α_1 from 0.2 to 3.0 in increments of 0.02 for each one of the four air-pollution (AP) models implemented into SMARTS. (The Huelva area is heavily industrialized and includes a chemical park with refineries, which is the biggest one in Spain; as such, local air pollution episodes are to be expected). The values obtained after the previous fit (#3) are used as inputs to Fit #4. Additionally, the ozone content is still defaulted to $u_o = 0.34$ cm.

3.4. Step 4

This step's goal is to refine the ozone content through a fifth iterative fit (#5), where a short spectral band is selected (513.9 nm to 674.9 nm) and u_o is progressively increased from 0.28 cm to 0.365 cm in increments of 0.005 cm, while the others quantities are set to their previously found values: PW(#3), AOD₅₀₀(#3), α_1 (#4), α_2 (#3), and AP(#4).

3.5. Step 5

Once the ozone content is evaluated, the calculation of α_1 and the AP model is improved in a sixth iterative process (Fit #6), for which the selected spectral band (353.2–497.1 nm) is wider than that of Fit #4, while the number of wavelengths is increased from 18 to 44, and the spectral step is somewhat reduced. Now, α_1 is varied from α_1 (#4) − 0.6 to α_1 (#4) + 0.6 in increments of 0.01 for each of the four AP models.

3.6. Step 6

Finally, a last iteration (Fit #7) is performed in an attempt to improve the accuracy of the two critical aerosol parameters (AOD₅₀₀ and α_2), knowing the more realistic estimates for ozone, water vapor, and AP model obtained in previous steps. The spectral band is now 513.9–1037.4 nm and involves 158 wavelengths in the case of the MS-700N instrument. AOD₅₀₀ is varied from AOD₅₀₀(#3) − 0.01 to AOD₅₀₀(#3) + 0.01 in increments of 0.001, whereas α_2 is varied from α_2 (#3) − 0.1 to α_2 (#3) + 0.1 in increments of 0.01.

The overall input-fitting process and the successive steps are summarized in the flowchart shown in Figure 7. Remarkably, once the SMARTS inputs are properly evaluated for a given measured spectrum, it is then possible to obtain the extended (280–4000 nm) tilted global spectrum incident on a PV module, thus providing the necessary information to evaluate its output and performance.

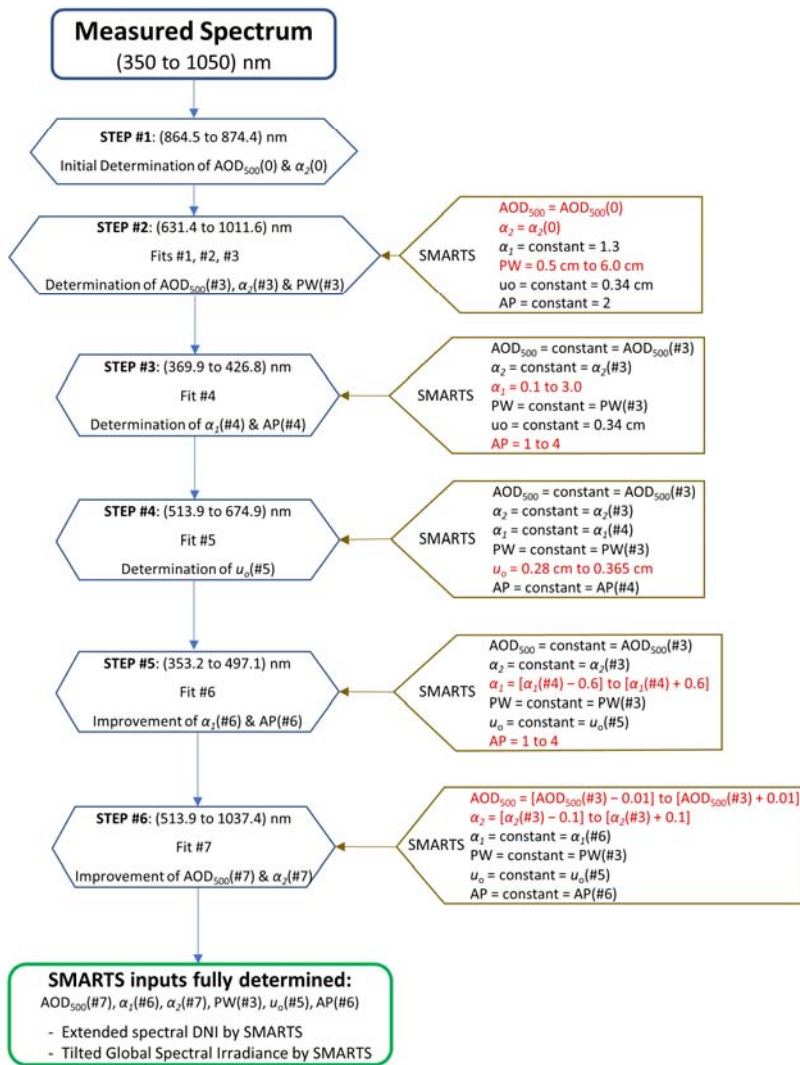


Figure 7. Flowchart of the methodology developed in this work. The measured spectrum is obtained with an EKO MS-700N spectroradiometer. Six steps are used to undertake seven fits where the input values of the SMARTS model are fixed iteratively to mimic the resulting modelled direct spectrum to the measured one. Once the inputs to SMARTS are determined, other spectral irradiance components of interest for the evaluation of PV technologies, such as the tilted global spectral irradiance, can be determined. The red letters in the brown boxes denote the SMARTS inputs to be varied in the fitting process, whereas the black letters correspond to those inputs with a constant value in the fitting process.

4. Results

The procedure has been applied to a variety of situations during the whole experimental period. For the sake of brevity, only results pertaining to two contrasting atmospheric situations are detailed below. Each situation has been chosen randomly among a large pool of “very clear days” and “very hazy days”, i.e., very low and high AOD, respectively. This is key here because the direct spectrum is mostly impacted by AOD [18]. The results for all the other days that have been tested are similar to those presented here.

The diurnal evolution of the 1-min measured global, diffuse, and direct broadband irradiances is shown in Figure 8 for two contrasting days. It is apparent that differing atmospheric conditions existed during the cloudless parts of the two days, mostly related to changes in AOD. More precisely, the second day was hazier (i.e., had a higher AOD) than the first one, which translates into lower direct and higher diffuse irradiances. The first day was cloudy until ≈ 0930 UT. The cloudless periods of the two days have been selected

after visual verification using the 1-min, all-sky images, as illustrated in Figure 9 for three different instants of each day. It is noted that, because of the hazier conditions, the second day's sky colour is whiter than that of the first day. Moreover, a thin cloud (delimited by a blue line in the top left picture) was in front of the sun at 1000 UT of the first day. This was expected to lead to higher and erroneous estimates of AOD. Nevertheless, this instance was analysed for further reference.

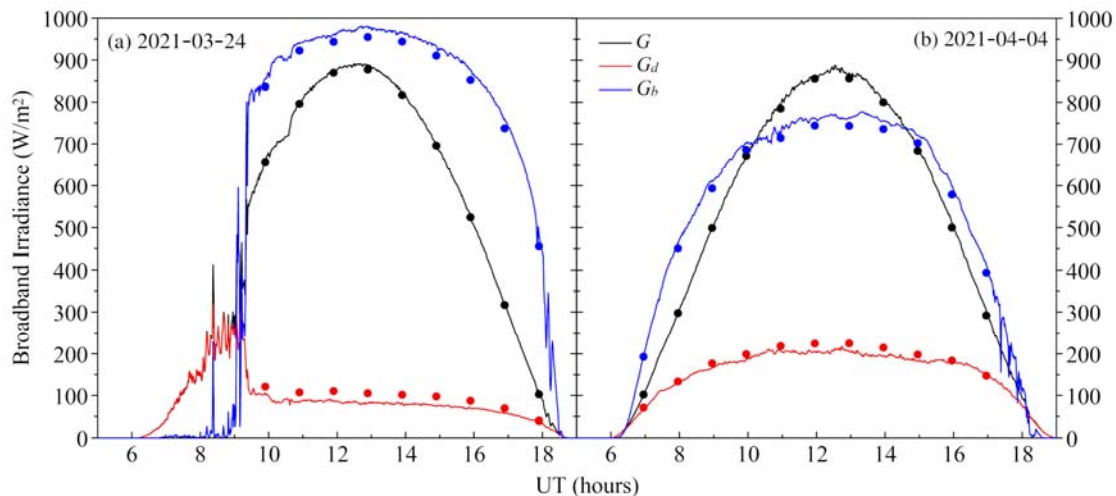


Figure 8. Diurnal variation of measured global (G), diffuse (G_d), and direct (G_b) broadband irradiances (solid lines) for two days selected to test the reliability of the method developed to extend the direct spectrum: (a) 2021-03-24; (b) 2021-04-04. The corresponding broadband values derived from the extended SMARTS spectra are also shown as dots. In the left plot, no such results are reported before 0930 UT because of cloudiness ($G_b \approx 0$).

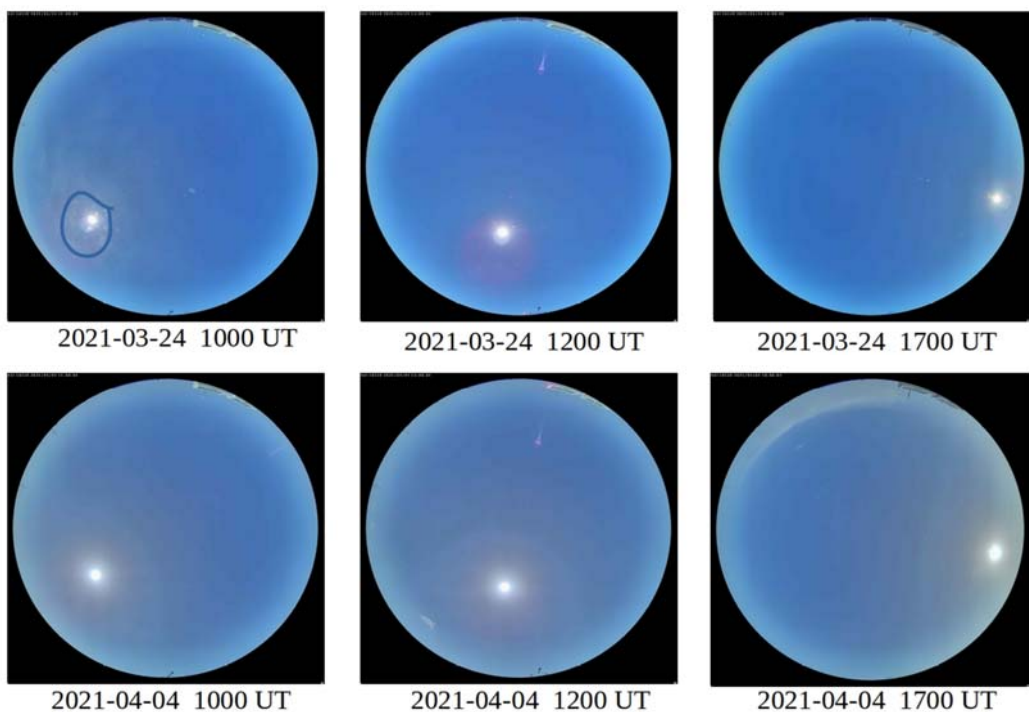


Figure 9. Sky pictures obtained with the all-sky imager at three instants during the two test days. A thin cloud (delimited by a blue line in the top left image) was in front of the sun at 1000 UT of the first day.

The SMARTS-derived spectrum's accuracy is evaluated by following the three independent procedures described below: (1) directly comparing the measured and estimated spectra; (2) comparing the measured and estimated broadband irradiances; (3) comparing the values of the estimated atmospheric parameters to those provided by a ground-based sunphotometer installed at the nearby AERONET site of El Arenosillo.

4.1. Spectrum Comparisons

Figure 10a shows the measured direct spectrum along with the fitted spectral irradiance simulated by SMARTS for three different instants (0900, 1200, and 1700 UT) on 2021-03-24. The good agreement between the measured and modelled spectra is remarkable. To better evaluate the low deviations observed, Figure 10b provides a scatterplot of the spectral estimates versus the measured ones. Note the low scatter around the ideal straight line 1:1 of perfect fit. In fact, the root-mean-square errors (RMSEs) for almost all analysed instants are < 2 % for their 212 common wavelengths. The results found for the other day, 2021-04-04, are similar but are not shown for brevity.

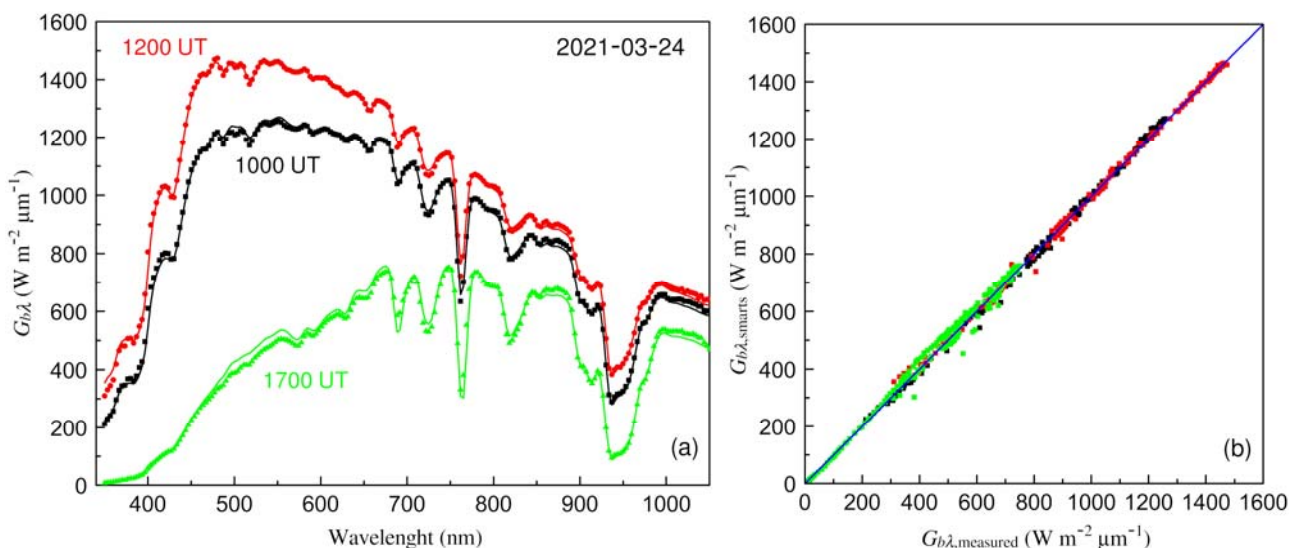


Figure 10. (a) Spectra measured with the EKO-MS700N spectroradiometer (dots) and estimated with SMARTS (lines) using the iterative procedure proposed here for the three instants of test day 24 March 2021 shown in Figure 9; (b) Estimated vs. measured spectral irradiance values corresponding to the same spectra considered in (a). The 1:1 diagonal of perfect fit is also shown.

Figure 11 compares the spectral irradiance distributions from the spectroradiometer to the SMARTS-based estimates (after smoothing to match the instrument's resolution) using the iterative procedure described above for day 2021-04-04 at 1000 UT. Again, the good agreement between these spectra is remarkable. In addition, Figure 11 also shows the SMARTS-derived spectrum at its native resolution of 0.5–5.0 nm between 280 nm and 4000 nm (2002 wavelengths). This extended version of the simulated spectrum significantly improves the resolution of the original experimental spectrum, which is a desirable feature in various applications and is necessary to accurately evaluate the corresponding broadband irradiance. Figure 7 shows such broadband values for the three irradiance components: total G , diffuse G_d , and direct G_b . Although a slight tendency to overestimate AOD seems to occur mainly in the middle part of the day (resulting in the direct and diffuse components being underestimated and overestimated, respectively), it is concluded that the agreement is more than satisfactory. This suggests that the proposed procedure is already reliable and efficient, at least for the range of atmospheric conditions investigated here.

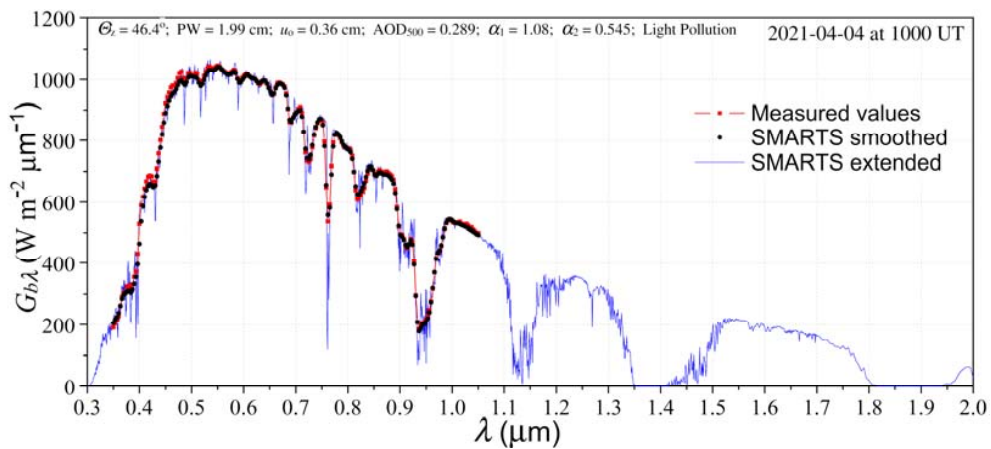


Figure 11. Spectral irradiances at 1000 UTC of 2021-04-04. The retrieved values of some atmospheric quantities used as SMARTS inputs are also indicated, along with the zenith angle (Θ_z).

4.2. AERONET Comparison

Although a complete analysis and comparison between the atmospheric characteristics derived in this work to those observed by a reference AERONET instrument is beyond the scope and extent of this work, a first and brief comparison between the two sets of values is discussed in this subsection for further reference.

Figure 12 shows the diurnal variations of the retrieved values of PW, AOD_{500} , α_1 , and α_2 throughout the two test days. The AOD_{500} and PW estimates constitute a rather satisfactory match for the reference AERONET observations. This remarkable result is further confirmation of the adequacy of the retrieval method proposed here and suggests that a well-calibrated tracking spectroradiometer sensing the direct spectrum can be reasonably used as a substitute for a sunphotometer. Interestingly, the good agreement aforementioned for AOD_{500} and PW is somewhat independent from the agreement found above for both spectral and broadband irradiances, because disparate sets of values can fortuitously be obtained if any one of the iteration processes leads to a local optimum rather than the true optimum. This adverse situation would prevent the iteration results from being similar to the AERONET retrievals, overwhelmingly considered in the literature as ‘ground-truth’ values. Hence, this AERONET-based validation constitutes a stringent way to evaluate the robustness and reliability of this new methodology.

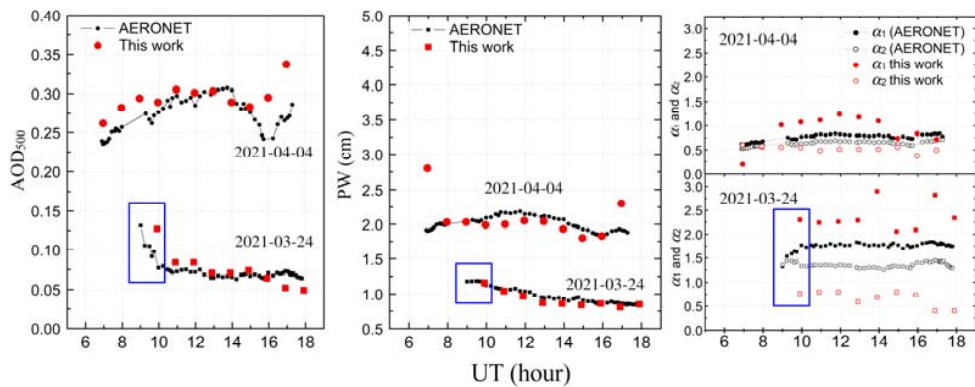


Figure 12. Retrieval of atmospheric constituents (AOD_{500} , PW, α_1 , and α_2) and their diurnal variation for the two test days of Figure 5. The blue rectangles denote instants when a thin cloud was occulting the sun, as shown in Figure 7. This circumstance induces an artificial increase in the retrieved AOD_{500} at Huelva, while no such cloudiness was simultaneously present at El Arenosillo.

As revealed in Figures 8 and 9, some cloudiness interfered with the experiment during short periods of one test day. The method described above to retrieve the key

atmospheric variables was conducted regardless, conditional to a non-zero direct irradiance. As expected, the retrieved AOD_{500} was incorrectly too high since the sun's disc is partially masked by a thin cloud, which adds its own optical depth. If such atmospheric retrievals were the main goal here, an *a posteriori* cloud-screening method would be necessary, such as the one routinely conducted on the AERONET raw data. Here, however, this issue is not a critical problem because the aim is to mimic the actual incident spectra on PV modules, even if affected by thin clouds.

In contrast with the good results mentioned above for AOD and PW, the Ångström exponents exhibit significant discrepancy, particularly during 2021-03-24. This appears to be related to the difficulty of obtaining a good representative value for these variables separately, possibly owing to the limited number of wavelengths for the two spectral bands. A single α value for the whole spectrum would simplify calculations and could be a better option; however, this has not been explored yet. From a different standpoint, it is also known that the determination of the Ångström parameter is difficult when AOD is low and generally prone to errors [31]. This can explain why their AERONET retrievals differ depending on the specific spectral band (and number of wavelengths) used for their derivation. Additional studies are definitely needed to improve this specific retrieval. Fortunately, though, any reasonable error here does not significantly impact the robustness of the extended spectra, as shown in Figure 11.

5. Conclusions

Low-cost spectroradiometers are currently being manufactured to monitor the spectral solar irradiance and are frequently used for PV research purposes at many solar laboratories. A usual drawback of these devices is their limited spectral range and/or relatively coarse optical resolution. These issues might hinder their usefulness in specific applications, such as the retrieval of atmospheric parameters or the study of PV spectral effects, where a wider spectral band is required because the spectral response of the PV cells under scrutiny extends beyond the range covered by the spectroradiometer.

The novel methodology proposed here offers an efficient and accurate way to extend the direct spectrum observed by spectroradiometers under clear-sky conditions. Both the spectral range and resolution of the original measured spectrum are improved using the simulations provided by the SMARTS spectral code. To that effect, an iterative procedure is developed to estimate the most important SMARTS atmospheric inputs through a succession of least-square fits. Once these SMARTS inputs are established, direct spectra ranging from 280 nm to 4000 nm and with a resolution of 0.5 nm to 5.0 nm (depending on waveband) can be simulated. This is particularly useful if spectra are needed for the other (diffuse and global) solar radiation components, or are needed for tilted surfaces, which is particularly important in the case of PV studies.

The results obtained here have also shown that, in addition to obtaining accurate spectral simulations, the new methodology is able to provide reliable estimates for the essential atmospheric quantities, such as precipitable water or aerosol optical depth at 500 nm. Ultimately, this suggests that tracking spectroradiometers sensing the direct spectrum could be used to monitor atmospheric constituents with an accuracy potentially comparable to that of sunphotometers under cloudless conditions.

Nevertheless, this procedure still needs refinements and to be further validated using data from a variety of locations, during longer periods, and with a wider range of atmospheric conditions. Optimization of the iteration algorithms will also be necessary to decrease the computation time, which is still substantial.

Author Contributions: Conceptualization, G.L., F.J.B. and C.A.G.; software J.P., J.A.-M. and P.F.; measurements, G.L., A.M. and M.I.E.-L.; data analysis, G.L., C.A.G., J.P., N.M.-C., A.M. and P.F.; writing—original draft preparation, all authors. All authors have read and agreed to the published version of the manuscript.

Funding: This research was supported by the Spanish Ministry of Economy, Industry, and Competitiveness [project PVCastSOIL N° ENE2017-83790-C3-1-2-3-R], in collaboration with the European Regional Development Fund. Also, the Authors want to acknowledge the project MAPV-Spain, with reference PID2020-118239RJ-I00, financed by the Ministerio de Ciencia e Innovación, and co-financed by the European Regional Development Fund. A. Marzo thanks for the Ramón y Cajal contract (RYC2021-031958-I), funded by the Spanish Ministerio de Ciencia e Innovación MCIN/AEI/10.13039/501100011033 and by the European Union “NextGenerationEU/PRTR”. Authors also acknowledge ANID/FONDAP/15110019 “Solar Energy Research Center”, SERC-Chile.

Data Availability Statement: The SMARTS software can be requested from <https://solarconsultingservices.com/smarts.php> (last accessed on 17 March 2023). Database is private.

Acknowledgments: The Authors thank to B.N. Holben, Victoria Cachorro, and Margarita Yela for their effort in establishing and maintaining the AERONET site at El Arenosillo. This work is dedicated to the memory of our dear colleague and friend Francisco Javier Batlles Garrido (1959–2022).

Conflicts of Interest: The authors declare no conflict of interest.

References

1. Ishii, T.; Otani, K.; Takashima, T. Effects of solar spectrum and module temperature on outdoor performance of photovoltaic modules in round-robin measurements in Japan. *Prog. Photovolt. Res. Appl.* **2010**, *19*, 141–148. [[CrossRef](#)]
2. Marzo, A.; Ferrada, P.; Beiza, F.; Besson, P.; Alonso-Montesinos, J.; Ballestrín, J.; Román, R.; Portillo, C.; Escobar, R.; Fuentealba, E. Standard or local solar spectrum? Implications for solar technologies studies in the Atacama Desert. *Renew. Energy* **2018**, *127*, 871–882. [[CrossRef](#)]
3. Jessen, W.; Wilbert, S.; Gueymard, C.A.; Polo, J.; Bian, Z.; Driesse, A.; Habte, A.; Marzo, A.; Armstrong, P.; Vignola, F.; et al. Proposal and Evaluation of Subordinate Standard Solar Irradiance Spectra for Applications in Solar Energy Systems. *Solar Energy* **2018**, *168*, 30–43. [[CrossRef](#)]
4. Fernández, E.F.; Almonacid, F.; Ruíz-Arias, J.A.; Soria-Moya, A. Analysis of the spectral variations on the performance of high concentrator photovoltaic modules operating under different real climate conditions. *Sol. Energy Mater. Sol. Cells* **2014**, *127*, 179–187. [[CrossRef](#)]
5. Alonso-Abella, M.; Chenlo, F.; Nofuentes, G.; Torres-Ramírez, M. Analysis of spectral effects on the energy yield of different PV (photovoltaic) technologies: The case of four specific sites. *Energy* **2014**, *67*, 435–443. [[CrossRef](#)]
6. Smestad, G.P.; Germer, T.A.; Alrashidi, H.; Fernández, E.F.; Dey, S.; Brahma, H.; Sarmah, N.; Ghosh, A.; Sellami, N.; Hassan, I.A.I.; et al. Modelling photovoltaic soiling losses through optical characterization. *Nat. Sci. Rep.* **2020**, *10*, 58. [[CrossRef](#)] [[PubMed](#)]
7. Qasem, H.; Betts, T.R.; Müllejans, H.; AlBusairi, H.; Gottschalg, R. Dust-induced shading on photovoltaic modules. *Prog. Photovolt Res. Appl.* **2014**, *22*, 218–226. [[CrossRef](#)]
8. Al Shehri, A.; Parrott, B.; Carrasco, P.; Al Saiari, H.; Taie, I. Impact of dust deposition and brush-based dry cleaning on glass transmittance for PV modules applications. *Solar Energy* **2016**, *135*, 317–324. [[CrossRef](#)]
9. Olivares, D.; Ferrada, P.; Marzo, A.; Llanos, J.; Miranda-Ostoic, C.; del Campo, V.; Bravo, S.; Fuentealba, E. Microstructural analysis of the PV module cementation process at the Solar Platform of the Atacama Desert. *Sol. Energy Mater. Sol. Cells* **2021**, *227*, 111109. [[CrossRef](#)]
10. Elminir, H.K.; Ghitas, A.E.; Hamid, R.H.; El-Hussainy, F.; Beheary, M.M.; Abdel-Moneim, K.M. Effect of dust on the transparent cover of solar collectors. *Energy Conv. Manag.* **2006**, *47*, 3192–3203. [[CrossRef](#)]
11. Hegazy, A.A. Effect of dust accumulation on solar transmittance through glass covers of plate-type collectors. *Ren. Energy* **2001**, *22*, 525–540. [[CrossRef](#)]
12. López, G.; Gueymard, C.A.; Polo, J.; Martín-Chivelet, N.; Alonso-Montesinos, J.; Marzo, A.; Batlles, F.J.; Vela, N.; Barbero, J. Assessing spectral mismatch factors from solar spectral measurements under clear and hazy conditions. In Proceedings of the 36th EU PVSEC Conference, Marseille, France, 9–13 September 2019. [[CrossRef](#)]
13. Nofuentes, G.; García-Domingo, B.; Muñoz, J.V.; Chenlo, F. Analysis of the dependence of the spectral factor of some PV technologies on the solar spectrum distribution. *Appl. Energy* **2014**, *113*, 302–309. [[CrossRef](#)]
14. Polo, J.; Alonso-Abella, M.; Martín-Chivelet, N.; Alonso-Montesinos, J.; López, G.; Marzo, A.; Nofuentes, G.; Vela, N. Typical Meteorological Year methodologies applied to solar spectral irradiance for PV applications. *Energy* **2020**, *190*, 116453. [[CrossRef](#)]
15. Pelland, S.; Gueymard, C.A. Validation of Photovoltaic Spectral Effects Derived from Satellite-Based Solar Irradiance Products. *IEEE J. Photovolt.* **2022**, *12*, 1361–1368. [[CrossRef](#)]
16. Núñez, R.; Victoria, M.; Askins, S.; Antón, I.; Domínguez, C.; Herrero, R.; Sala, G. Spectral impact on multijunction solar cells obtained by means of component cells of a different technology. *Photovolt. IEEE J. Photovolt.* **2018**, *8*, 646–653. [[CrossRef](#)]
17. Boisvert, J.; Law, D.; King, R.; Bhusari, D.; Liu, X.; Mesropian, S.; Larrabee, D.; Woo, R.; Edmondson, K.; Krut, D.; et al. Development of advanced space solar cells at Spectrolab. In Proceedings of the 35th IEEE Photovoltaic Specialists Conference, Honolulu, HI, USA, 20–25 June 2010. [[CrossRef](#)]

18. Gueymard, C.A. The SMARTS spectral irradiance model after 25 years: New developments and validation of reference spectra. *Solar Energy* **2019**, *187*, 233–253. [[CrossRef](#)]
19. Berk, A.C.; Anderson, G.P.; Bernstein, L.S.; Acharya, P.K.; Dothe, H.; Matthew, M.W.; AdlerGolden, S.M.; Chetwynd, J.H.; Richtsmeier, S.C.; Pukall, B.; et al. MODTRAN4 radiative transfer modeling for atmospheric correction. In Proceedings of the Optical Spectroscopic Techniques and Instrumentation for Atmospheric and Space Research III, SPIE vol. 3756, Denver, CO, USA, 19–21 July 1999. [[CrossRef](#)]
20. Mayer, B.; Kylling, A. The libRadtran software package for radiative transfer calculations—Description and examples of use. *Atmos. Chem. Phys.* **2005**, *5*, 1855–1877. [[CrossRef](#)]
21. Gueymard, C.A. Interdisciplinary applications of a versatile spectral solar irradiance model: A review. *Energy* **2005**, *30*, 1551–1576. [[CrossRef](#)]
22. Gueymard, C.A. Prediction and validation of cloudless shortwave solar spectra incident on horizontal, tilted, or tracking surfaces. *Solar Energy* **2008**, *82*, 260–271. [[CrossRef](#)]
23. Salmon, A.; Quiñones, G.; Soto, G.; Polo, J.; Gueymard, C.; Ibarra, M.; Cardemil, J.; Escobar, R.; Marzo, A. Advances in aerosol optical depth evaluation from broadband direct normal irradiance measurements. *Solar Energy* **2021**, *221*, 206–217. [[CrossRef](#)]
24. Sorribas, M.; de la Morena, B.A.; Wehner, B.; López, J.F.; Prats, N.; Mogo, S.; Wiedensohler, A.; Cachorro, V.E. On the sub-micron aerosol size distribution in a coastal-rural site at El Arenosillo Station (SW—Spain). *Atmos. Chem. Phys.* **2011**, *11*, 11185–11206. [[CrossRef](#)]
25. Holben, B.N.; Eck, T.F.; Slutsker, I.; Tanre, D.; Buis, J.P.; Setzer, A.; Vermote, E.; Reagan, J.A.; Kaufman, Y.; Nakajima, T.; et al. AERONET—A federated instrument network and data archive for aerosol characterization. *Remote Sens. Environ.* **1998**, *66*, 1–16. [[CrossRef](#)]
26. Escalona-Llaguno, M.I.; López, G.; Ortega, G.; Alonso-Montesinos, J.; Polo, J.; Ballestrín, J. Automatic discrimination between haze and cloudiness in all sky camera images. In Proceedings of the 10^a Asamblea Hispano Portuguesa de Geodesia y Geofísica (10AHPGG), Toledo, Spain, 28 November–1 December 2022. In press.
27. Bright, J.M.; Sun, X.; Gueymard, C.A.; Acord, B.; Wang, P.; Engerer, N.A. Bright-Sun: A globally applicable 1-min irradiance clear-sky detection model. *Renew. Sustain. Energy Rev.* **2020**, *121*, 109706. [[CrossRef](#)]
28. EUMETSAT. Available online: <https://view.eumetsat.int/productviewer?v=default> (accessed on 3 March 2023).
29. Gueymard, C.A. Revised composite extraterrestrial spectrum based on recent solar irradiance observations. *Solar Energy* **2018**, *169*, 434–440. [[CrossRef](#)]
30. Gueymard, C.A.; Myers, D.; Emery, K. Proposed reference irradiance spectra for solar energy systems testing. *Solar Energy* **2002**, *73*, 443–467. [[CrossRef](#)]
31. Gueymard, C.A. *Clear-Sky Radiation Models and Aerosol Effects. Solar Resources Mapping. Green Energy and Technology*, 1st ed.; Springer: Cham, Switzerland, 2019; pp. 137–182. [[CrossRef](#)]

Disclaimer/Publisher’s Note: The statements, opinions and data contained in all publications are solely those of the individual author(s) and contributor(s) and not of MDPI and/or the editor(s). MDPI and/or the editor(s) disclaim responsibility for any injury to people or property resulting from any ideas, methods, instructions or products referred to in the content.